
Article:
Rahimov, E. orcid.org/0000-0001-9557-5808, Watson, M., Hadjisoteriou, A. et al. (1 more author) (2022) Investigation of wear mechanisms in AlSi-polyester abradable - Ti(6Al4V) blade contacts using stroboscopic imaging. Wear, 494-495. 204207. ISSN 0043-1648

https://doi.org/10.1016/j.wear.2021.204207

Investigation of wear mechanisms in AlSi-polyester abradable - Ti(6Al4V) blade contacts using stroboscopic imaging

Eldar Rahimov*, Michael Watson, Andreas Hadjisoteriou, Matthew Marshall[1]

[1] Department of Mechanical Engineering, The University of Sheffield, Mappin Street, Sheffield S1 3JD, UK

Corresponding author.
Eldar Rahimov
E201-23
3 Portobello St, Engineering Heartspace
The University of Sheffield,
S1 4DT
E-mail address: erahimov1@sheffield.ac.uk
Tel.: +447478339044

Keywords: Abradable testing; Wear testing; Stroboscopic imaging; Profilometry

Summary

Abradable linings in aero engines have been an area of research interest over the past few decades as small reductions in clearances between stationary and rotating parts can lead to large increases in engine efficiency. The work performed in this article focuses on characterising the blade wear behaviour in contacts between Ti (6Al 4V) blades and AlSi-polyester abradables. This was done by performing three abrasion tests on the new test rig developed at the University of Sheffield. Tests have been performed on the AlSi-polyester abradables of the same nominal hardness over two incursion rates – 0.02µm/pass and 0.2 µm/pass and two blade tip speeds – 85m/s and 170m/s. The front-on stroboscopic imaging technique was used for these tests, which allowed capturing images of the entire blade front for a number of blade strikes during a test. It was found that at the incursion rate of 0.02µm/pass, both adhesions to the blade surface and blade wear were observed across the blade width. It was observed that adhesions were more likely to gradually wear off rather than fracture at 0.02µm/pass, and, fracture at 0.2µm/pass. Tested surface profiles were obtained using an Alicona non-contact measurement system. This allowed the comparison of the blade profile results from the blade images to the surface of the respective tested abradable sample. It was concluded that adhesions that fractured could contribute to the localized gaps between the final blade and the final abradable surface where such adhesions have fractured close to the end of a test. Further testing areas have been identified such as the investigation into the effects of parameters such as incursion rate of a blade into an abradable, blade tip speed and abradable hardness on the results. The developed front-on imaging system also opened a possibility to investigate in-situ the rub performance of blades of varying tip geometry.

Nomenclature

P_d – perpendicular projection length of the disk edge from the centre of the disk

P_b – perpendicular projection length of the edge of the blade from the centre of the disk

l_d – radial length of the disk (i.e. disk edge length from the centre of the disk)

l_b – combined radial length of the disk and the blade edge (i.e. the blade edge length from the centre of the disk)

l_{du} – unobserved part from the centre of the disk to the field of view of camera limit

l_{do} – observed projection of the disk edge

l_{bo} – observed blade edge profile

b_d – length of the flat section at the edge of the disk

b_b – blade thickness

R_{de} – radius of disk edge curvature

θ – angle of deviation of blade position on an image from the vertical

l_{rtotal} – rub length

i – incursion rate in m/pass

n_p – incursion number from the start of the test

$n_{current}$ – number of incursions completed by the time of the image

R_a – average height along a line

R_q – root-mean-squared height along a line

R_p – maximum peak height

R_v – maximum valley depth

R_z – height of the blade roughness profile (sum of the absolute values of R_p and R_v)

S_a – average height of selected area

S_q – root-mean-square height of selected area

S_p – maximum peak height of selected area

S_v – maximum valley depth of selected area

S_z – height of the selected area (sum of the absolute values of S_p and S_v)

1 INTRODUCTION

Abradable materials are sprayed onto the casing of aero-engine compressor stages to minimise aerodynamic losses. Without abradable materials, contact between a blade and the casing would result in blade wear and increased clearance. With the abradable materials sprayed onto the casing, in case of such a contact, they would wear in preference to the blade. Even if the blade is returned to the original radial position, the created gap is not detrimental to the aerodynamic performance as this gap is still sufficiently sealed by the abradable material to both sides of the blade.

Initial sealing is achieved during aero-engine running and handling, where the engine is tested at its full speed before the start of its service. During this procedure, blades will expand with respect to the lined casing due to the mismatch of the thermal expansion between the blades and the casing and the centrifugal forces acting on the blades. Blades will then cut a path in an abradable material creating the initial seal (1).

1.1 Background

Research into abradable linings is driven by two main areas: research into the linings' nominal mechanical properties and research into the tribological properties of the contacts between the abradables and the aero-engine blades.

Common techniques used to characterise abradable mechanical properties are hardness testing, sliding wear volume (2) and scratch testing (3). However, mechanical properties tests do not allow to fully understand and predict the contact mechanics between an abradable and a rubbing blade as they fail to reproduce contact conditions observed within aero-engine compressors. Such contacts require more factors to be considered such as blade speed, incursion rate of a blade into an abradable material, abradable phase distributions, temperatures and contact fracture mechanisms.

Abradable – blade contacts have been further investigated using simulation models and purpose-built testing rigs. The abradable-blade contact simulations have primarily focused on understanding the blade dynamics in the abradable-blade contacts and the effect of non-linearity on such contacts (4), (5). Some attempts were also made to simulate common wear mechanisms observed in aero-engines (6).

Most of the work focused on understanding the wear mechanisms in abradable – blade contacts has been performed using scaled and full-scale experimental rigs. This article considers wear mechanisms in contacts involving AlSi-polyester abradables and hence, only results relevant to AlSi-based abradables are going to be highlighted.

Borel et al. (7) produced the first comprehensive list of wear mechanisms commonly seen in aero-engines compressors and created wear maps for the AlSi-plastic type abradables using the Sulzer Metco rig. Following on, Bounazef et al. (8) has performed characterization of AlSi-hBN abradables using the Sulzer Metco rig and found that high blade tip speeds and incursion rates led to reduced material transfer to the blade.

With a specific tribological focus on a scaled 200m/s rig at the University of Sheffield, Stringer et al. (9) and Fois et al. (10) have further investigated AlSi-hBN abradables. Stringer et al. (9) found that simultaneous wear of and adhesion to the blade occurred under certain testing conditions and Fois et al. (10) found that adhesive transfer at low incursion rate and cutting wear at high incursion rate were the observed wear mechanisms. Watson et al. also investigated AlSi-polyester and NiCrAl-bentonite abradables (11), where for AlSi-polyester a similar two-component wear mechanism was suggested based on incursion rate: adhesive and abrasive wear for low incursion rates and cutting mechanism for high incursion rates.

Latterly, Zhang et el. (12) investigated AlSi-polyester abradables using a high-speed rig developed at Zhejiang University. They found that AlSi-polyester abradable samples were soft enough to allow low blade wear and that incursion rate expressed as depth/pass had a great impact on the wear surface morphology.

Xue et al. also investigated AlSi-hBN abradables – titanium blades contacts using a rig developed at Chinese Academy of Sciences (13) (14) and found a strong effect of both speed and incursion rate on the observed wear mechanisms. Based on the post-test analysis they concluded that high-blade speed and low incursion rate were the requirements for increased coating transfer to the blade. There was also evidence that blade wear and adhesive transfer to the blade co-occurred for the test at 0.085μm/pass incursion rate and 90m/s blade speed.

Focusing on the incursion accommodation mechanisms, Mandard et al. (15) has looked at the AlSi-polyester coating using the rig developed at the French Aerospace Lab. He found debris release and compaction to be the primary mechanisms of

abradable thickness loss and reversible deformation to accommodate the remaining incursion depth. However, the incursion rate observed in that study was several orders of magnitude larger than in the majority of the other studies and hence, results are difficult to compare.

More recently, a rig was developed at Technische Universität Dresden with a capability to test blades of engine representative geometry and ability to vary the number of abradable segments from 1 to 20 presented by Nitschke et al. (16). However, only limited data is currently available from the tests performed using that rig.

In the above-mentioned articles wear mechanisms were commonly assessed by post-test investigation of blades and abradable samples. However, the limitations of using blade length and weight change measurements for wear mechanism classification have been shown by Stringer et al (9) for the cases where simultaneous blade wear and adhesive mechanisms occurred within a single test.

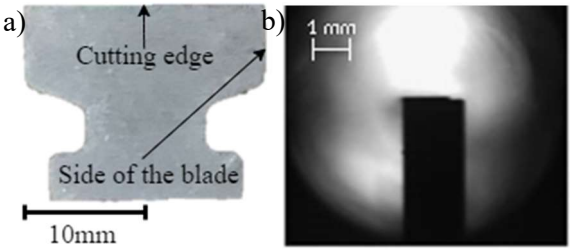

Figure 1 - a) an example of a blade used for testing, b) an image of a blade captured from the side during a test (10)

Additionally, in the works by Bounazef et al. (8) and Fois et al. (10) fracture of adhesions from a blade was observed suggesting that post-test analysis of blades might not be sufficient for classifying severity of adhesive wear. In the work by Fois et al. (10) using a side-on stroboscopic imaging allowed measurement of the maximum blade length throughout the entire test. However, as can be seen from Figure 1 by measuring from the side, it wasn't possible to tell at what exact position along the blade width adhesions occurred, what was the size of an adhesion in terms of its width and if there were only one or multiple different adhesions on the blade along its width at any given time.

In this work, a front-on stroboscopic imaging system is developed for the new test rig, where the entire blade width is seen to address the limitations of using the side-on imaging and post-test blade length measurements for wear mechanisms classification. Details about the design and operation of the rig and the front-on stroboscopic imaging system are given in the next section.

2 METHODOLOGY

The wear mechanisms observed in Ti(6Al 4V) blades – AlSi-polyester abradables contacts were investigated on a new test abradable rig, which includes a front-on imaging stroboscopic system to monitor the changes in blade length across the blade's entire width throughout the test.

2.1 Test Rig

The test rig consists of several components essential for performing an incursion test as shown in Figure 2 and Figure 3: a spindle, a stage, bearing supports, a disk, which is supported in between the front and the back bearings and a rig containment, which is built out of steel plates and steel blocks, which are filled with concrete on the inside. The spindle (GMN HSP170s - 30000/19) is controlled by the spindle inverter (Emerson SK 4401 HF). The spindle is cooled by the water chiller (Hyfra Chilly 45) and lubricated by an oil-air lubricating unit. Gaps in the spindle's casing are purged by a pressurised air supply (17).

The disk is connected to the spindle through a flexible coupling. The cutting and dummy (for disk balancing) blades are inserted into the disk slots that are located 180 degrees from each other. The maximum blade tip speed is 300m/s.

The stage is used to move abradable samples at a constant incursion speed towards the rotating disk. It consists of a front plate, which allows for attaching the force dynamometer and test samples on it, a ball screw (HD30406-MF-M-U2-20-C20B High Precision Linear Actuator Ball screw driven), a system of gearboxes resulting in a total gear ratio of 600:1 and a servo motor (KEB, 24.SM200-42B0), which is controlled by the rig computer through a stage inverter (KEB combivert F5 servo) (17).

The test rig instrumentation includes a front-on imaging system, a pyrometer (CTLM-3H1CF3-C8, Micro-Epsilon) and a dynamometer (Type 9347C 3-Component Force Link, Kistler). Details of the new front-on stroboscopic imaging system and the test procedure are given in the following sections.

2.2 Front-on Imaging System.

The stroboscopic system allows an image of the blade to appear stationary, as light is only on when the blade is in the position best suited for imaging

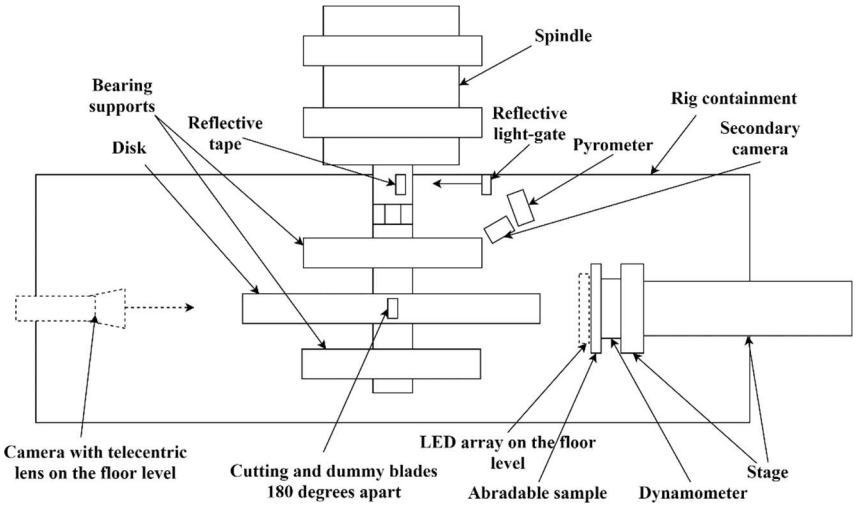

Figure 2 - The test rig diagram, top view

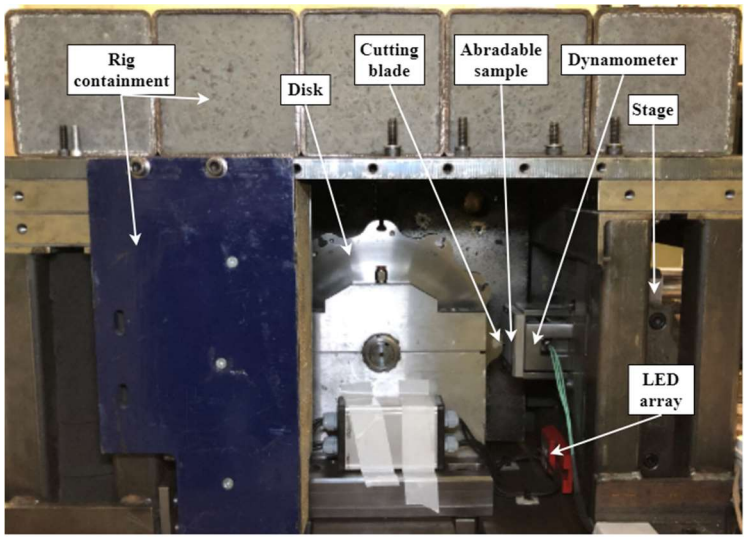

Figure 3 - The test rig image, side view

it. The system consists of the following parts: a reflective tape mounted on the shaft, a reflective sensor (Omron E3T-FD13), a LED strobe controller (Gardasoft PP880) fitted with a signal delay board, LEDs (SHARP GW5BTJ50K03 LED Module, MINI ZENIGATA Series, Cool White, 5000 K, 690 lm) and a camera (Basler ace - acA1300-60gm, 1.3M resolution, 5.3µm x 5.3µm pixel size) fitted with a telecentric lens (Edmund Optics 0.25X SilverTL™, combination of the camera and the lens leads to an image pixel size of 21.2µm x 21.2µm). LEDs are positioned directly opposite to the camera from the other side of the blade so that for the captured image, the blade is positioned on a line between the LED array and the camera. The set-up is illustrated in Figure 2.

The system works based on the following principle: the reflective sensor sees the reflective tape once per revolution of the shaft and sends a signal to the strobe controller. The strobe then turns on the LEDs with a pre-defined delay for a specified pulse width duration. The required delay is based on two factors: the angular position of the reflective tape on the shaft with respect to the cutting blade position, and the rotational speed of the shaft and the disk assembly. Additionally, the wire between the reflective sensor and the strobe controller box is shielded with a metal tape to prevent false triggers of the LEDs due to surrounding electrical noise.

An example raw image produced by the stroboscopic imaging system when the camera was exposed over one revolution of a blade is shown in Figure 4. The stroboscopic imaging technique is currently operational up to the speed of 170m/s, and the camera records at 60 frames/s, capturing approximately one image every 3 revolutions of the disk at this speed.

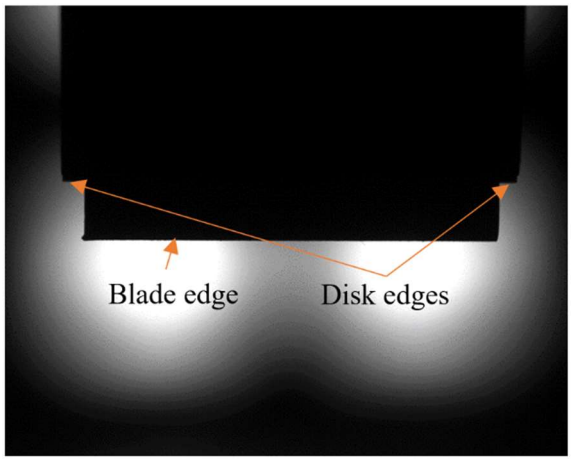

Figure 4 - The raw image of a spinning blade (at 4500 rpm) exposed over one revolution of a blade

2.3 Test Procedure and Rig Control

Before the start of a test, an abradable sample is mounted on the sample holder plate on the dynamometer, and cutting and dummy blades are secured in the disk using removable blade holders. A standard abradable sample and blade can be seen in Figure 5. The spindle inverter is then turned on and spindle and stage speeds controlled through a program developed in LabVIEW 2018 (National Instruments).

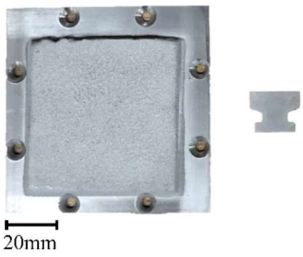

Figure 5 - A standard abradable sample and blade used for testing

2.3.1 Tests Parameters

The aim of this work is to investigate the effects of the incursion rate and the blade tip speed on the contact mechanics between Ti(6Al 4V) blades and AlSi-polyester abradables.

Three tests have been performed, and the incursion rates were selected as 0.02µm/pass and 0.2µm/pass (between 1.66µm/s and 33.2µm/s) and blade tip speeds as 85m/s and 170m/s. Incursion rates were selected at the lower end of the spectrum commonly used in literature, as it was previously shown that such conditions result in an increased adhesive transfer to the blade, which is the mechanism of primary interest in this work (10). The upper testing blade tip speed limit was guided by the current limit for the stroboscopic imaging system.

The summary of test conditions is shown in Table 1. For all the tests, AlSi-polyester abradables had a nominal hardness of approximately 70 on the HR15Y scale. All the tests were performed to an incursion depth of 1000µm. Combination of the testing parameters have resulted in the test duration variation from 30 seconds to 10 minutes. However, even for the shorter tests, representative contact temperatures would have been reached, as it was previously shown that flash temperatures can reach steady values within seconds (18; 19).

Test	Tested Blade	Abradable Sample	Blade Tip Speed / m/s	Incursion Rate/ µm/pass (µm/s)
1	Ti	AlSi-polyester 70HR15Y	85	0.02 (1.66)
2	Ti	AlSi-polyester 70HR15Y	85	0.2 (3.32)
3	Ti	AlSi-polyester 69.3HR15Y	170	0.2 (33.2)

Table 1 - The test conditions

2.4 Alicona Analysis

Post-test, surface images of approximately 27mm across the width and 17mm along the length of the wear track were recorded for each tested abradable sample using the Alicona SL (Bruker Alicona) equipment. Measurement area was limited by the size of the data feasible to be exported as a .txt file for post-processing in MATLAB.

2.5 SEM Blade Surface Measurements

Back-scattered SEM images of the tested blades were collected using the Desktop SEM TM3030 equipment for further analysis of blade adhesions and wear.

3 DATA PROCESSING

In this section, methods used to analyse images obtained using the stroboscopic system and abradable surface profiles obtained using the Alicona SL equipment are discussed. All the processing is shown on the example of data from the test at 85m/s blade tip speed and 0.2µm/pass incursion rate.

3.1 Front-on Camera Image Processing

Several steps were employed to get from a raw image to an extracted blade profile. These steps are

image cropping (Figure 6), three iterations of 2-D median filtering, image binarization, edge detection using the "Prewitt" method (Figure 7), blade vertical edge deterction (Figure 8) and finally blade profile extraction (Figure 9). The "Prewitt" method for edge detection was checked across a variety of image brightness conditions and it was shown to produce accurate and reliable results.

The blade is extracted such that it is within the limit defined by the eight points to the right of the leftmost vertical line and eight points to the left of the rightmost vertical line. This limit and the extracted blade profile are shown in Figure 9. Eight points were left on each side to allow for a variation in the vertical edges of the blades.

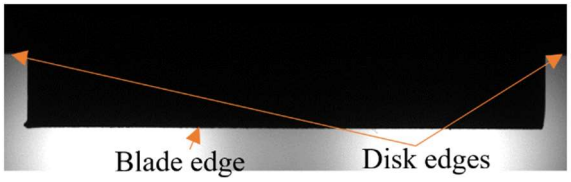

Figure 6 - The cropped image (original image shown in Figure 4)

Figure 7 - The detected edge using "Prewitt" method overlaid on the binarized image

Figure 8 – The detected vertical edges of the blade shown in orange

Figure 9 - The final blade profile in green overlaid on the binarized image with defined vertical limits shown in orange

3.2 Blade Length Referencing

Blade position changed on images due to variation in an angle at which blade image was captured as shown in Figure 10. This was due to uncertainty in the detection of reflection from the reflective tape. A referencing method has been developed to compensate for variation in blade position on the images.

Referencing works on the principle that the length from the centre of the disk to the edge of the disk is constant and so, disk edge should remain in the same position on the images. It is also assumed that any blade length change is uniform across the thickness of the blade.

Diagrams of the disk and the blade with respect to the camera are shown in Figure 10. The disk that is considered is not a perfect circle, but rather has a flat section, b_d, symmetric to both sides of the blade. The following equations can be derived from geometry:

$$P_d = l_d \cos(\theta) + \frac{b_d}{2}\sin(\theta) + R_{de}(1 - \cos(\theta))$$

Equation 1

where, P_d is the perpendicular projection length of the disk edge from the centre of the disk, l_d is the radial length of the disk (i.e. disk edge length from the centre of the disk), b_d is length of the flat section at the edge of the disk, R_{de} is the radius of disk edge curvature, and θ is the angle of deviation of the blade position on an image from the vertical, and:

$$P_b = l_b \cos(\theta) + \frac{b_b}{2}\sin(\theta)$$

Equation 2

Where P_b is the perpendicular projection length of the edge of the blade from the centre of the disk, l_b is the combined radial length of the disk and the blade edge (i.e. the blade edge length from the centre of the disk) and b_b is the blade thickness. P_d is obtained from extracting the position of the disk edges shown in Figure 6 for each image in the dataset. Detailed information on the extraction of P_d values is given in Appendix A. In the first equation, all other variables except for the angle of deviation from the vertical, θ, are known from geometry. This allows solution for θ as follows:

$$\theta = \text{acos}\left(\frac{P_d - R_{de}}{\sqrt{(l_d - R_{de})^2 + \left(\frac{b_d}{2}\right)^2}}\right) + \text{atan}\left(\frac{\frac{b_d}{2}}{l_d - R_{de}}\right)$$

Equation 3

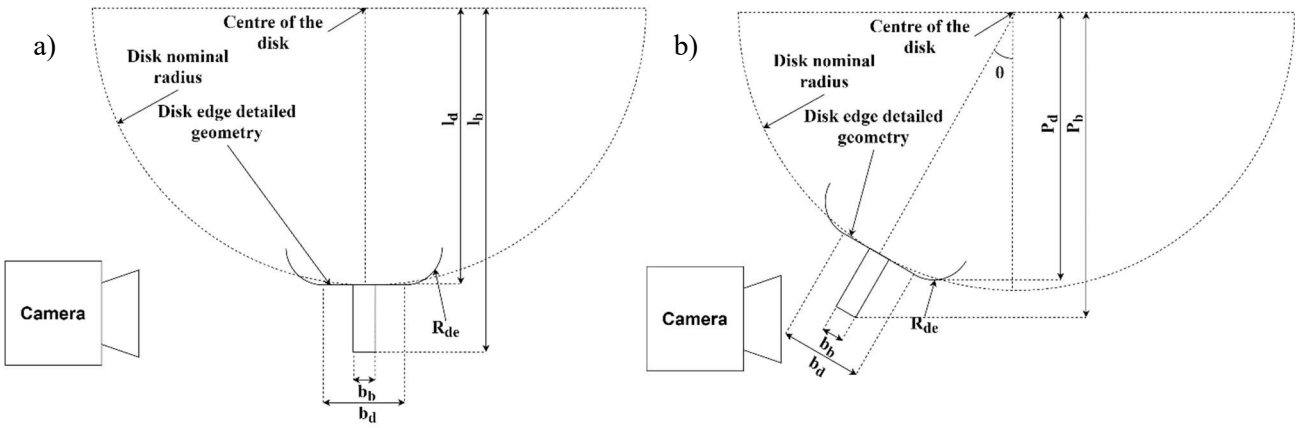

Figure 10 - The blade and the disk positions shown a) when blade is perpendicular to the camera, b) when blade is at an angle to the camera resulting in blade moving up on an image. Key variables required for the calculation of the referenced blade edge position are labelled on the diagram

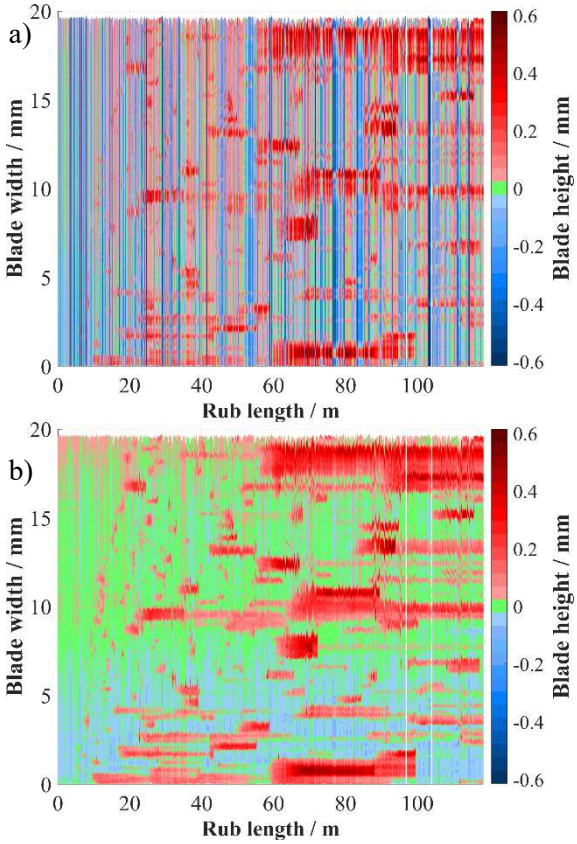

Figure 11 - a) The blade profile history map for the test at 0.2µm/pass and 85m/s – unreferenced, b) the blade profile history map for the test at 0.2µm/pass and 85m/s – referenced

Knowing θ, it is possible to solve Equation 2 for the length from the centre of the disk to the blade tip, l_b. The projected length of the blade from the centre of the disk to the blade tip, P_b, is then determined from the extracted blade profile shown in Figure 9 for each image in the dataset as follows:

$$l_b = \frac{P_b - \frac{b_d}{2}\sin(\theta)}{\cos(\theta)}$$

Equation 4

The blade height plotted against rub length is shown in Figure 11 for the unreferenced blade profiles (a) and the referenced blade profiles (b). These illustrate the effectiveness of the referencing procedure, as the noise created in the data set from the variation in blade position on the images is evident in Figure 11a and is removed in Figure 11b.

In Figure 11, blade height is given by the blade profiles vertical coordinates datumed to the mean height of the blade profile on the first image in a dataset and converted from pixels to mm. Blade width is given by the blade profiles horizontal coordinates converted from pixels to mm. Rub length is calculated as a sum of rub lengths per revolution of the disk for each revolution that was expected to be completed by the time of a given image and is defined as:

$$l_{rtotal} = \sum_{n_p=1}^{n_{current}} 2l_b \operatorname{acos}\left(\frac{l_b - in_p}{l_b}\right)$$

Equation 5

where l_{rtotal} is the rub length, i is the incursion rate in m/pass, l_b is in m, n_p is the revolution number from the start of a test and $n_{current}$ is the number of revolutions completed by the time of an image. Rub length is non-linearly related to time and blade revolution number. With increase in time, rub-length per revolution increases due to the arc of contact increasing with incursion depth; and so total rub length growths faster than time and revolution number.

Variation in the mean length of the blade at the start of the test (for the first 25 images) was considered to assess repeatability of the measurements. No significant wear/adhesion is expected to occur by this point, so all the variations are expected to be primarily due to uncertainty in the measurements. Standard deviation (standard uncertainty) of blade mean length values for the unreferenced data was found to be 123µm and for the referenced data 13µm. This further justifies the use of the referenced data. The size of one pixel on an image is 21.2µm (half-uncertainty is then 10.6µm). Assuming rectangular distribution for uncertainty due to rounding to the nearest pixel, standard uncertainty due to this source is then $10.6/\sqrt{3}$ = 6.1µm. The combined standard uncertainty for blade length results is then $\sqrt{13^2 + 6.1^2}$ = 14µm.

3.3 Theoretical Surface Profiles

It was observed on the raw data that some adhesions fractured from the blade. An additional blade profile was constructed to understand how the fractured adhesions contributed to the final tested abradable surface. This blade profile included the detached adhesions into its shape based on how deep they could have rubbed into the abradable material before they detached. This was done using the following procedure:

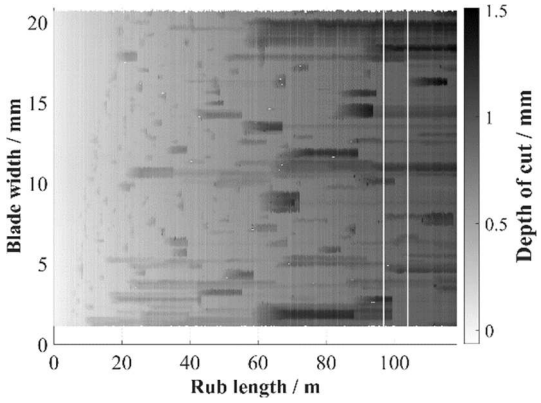

Figure 12 - The modified plot considering the current rub depth for the test at 0.2µm/pass and 85m/s

Each extracted blade profile had the difference between the final and the current rub depths subtracted from it to calculate how deep the blade would have rubbed into the abradable at each point along the blade width for this blade profile. Such a modified plot is shown in Figure 12. A blade profile based on the highest depth of cut value for each blade width position was then extracted.

It was also noted that some of the very long sharp adhesions existed only on one image, after which, they detached. To check if they contributed to the final abradable shape, an additional blade profile was created, which consisted of the third highest point for each blade width position. The third point was selected over the second one to ensure that for the case there are two short-lived sharp adhesions at the same location along the blade's width throughout a test, both are ignored. The expected abradable surface profile based on the highest depth of cut point is then referred to as the 1-point profile, and the profile based on the third highest point as the 3-points profile later in this work.

The final blade profile and the two constructed profiles are shown in Figure 13.

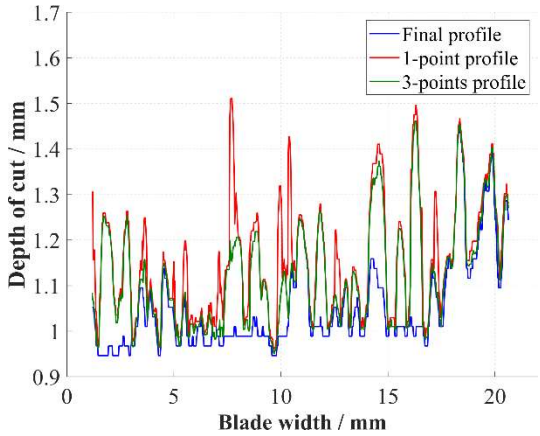

Figure 13 - The final and the two constructed blade profiles for the test at 0.2µm/pass and 85m/s

3.4 Adhesion Rates Analysis

Five lines (five were selected to ensure representative adhesion measurements for each test) were extracted for each test from the blade profile history maps in blade width locations where adhesions occurred. The selected lines for the test at 0.2µm/pass and 85m/s are shown with white dashed lines in Figure 14.

Each line was then plotted on a separate 2D plot and a 5-point Gaussian smoothing function was applied to reduce noise in the data. An example of such a line can be seen in Figure 15.

As shown in Figure 16, for each adhesion event four points were selected: two points where adhesion growth was linear for adhesion rate calculation (shown in blue) and two points for peak height and relative peak heights calculation (shown in green).

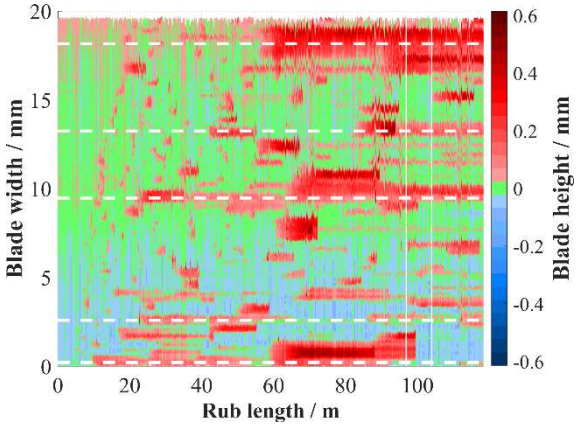

Figure 14 - Lines selected for further processing of adhesion rates

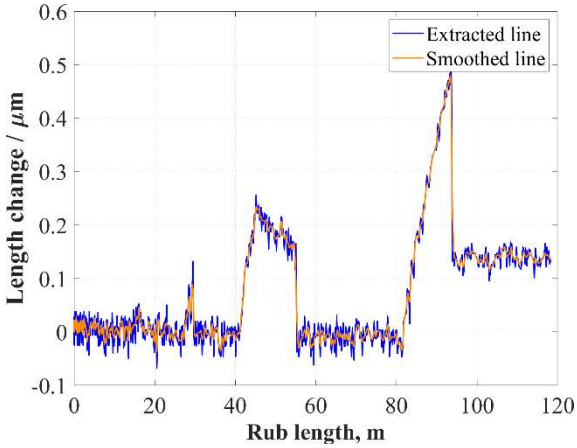

Figure 15 - Extracted and smoothed lines for blade width positon of 13.3mm

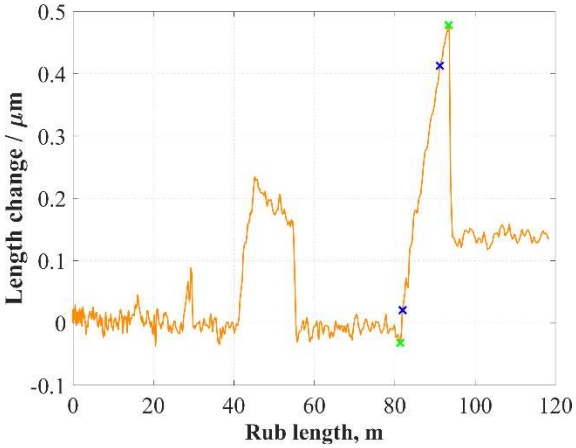

Figure 16 - Selected points

Histograms presented in section 5 were then created by calculating the mean (histogram height) and standard deviation value (error bars) of a dataset of all recorded adhesion events in a given test.

3.5 Alicona Surface Measurements

The approximate area (approximately 27mm x 17mm) selected for the analysis of each sample is shown in blue in Figure 17.

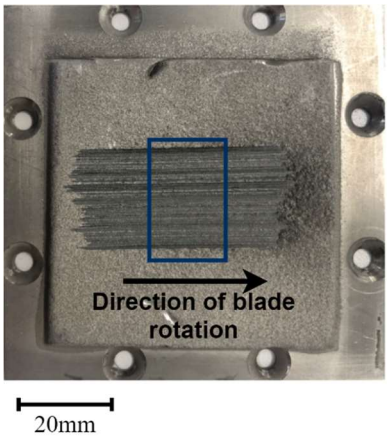

Figure 17 - The area selected for the Alicona analysis shown in blue

The recorded space to the left and the right of the rub width is removed in MATLAB, and the cropped surface plotted in plan view is shown in Figure 18.

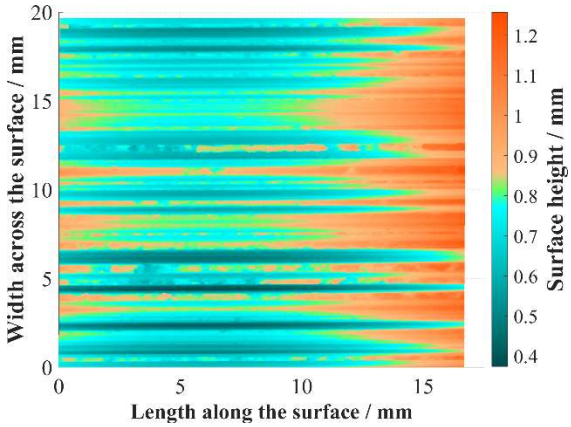

Figure 18 - The imported Alicona data

Curvature of the sample in the length direction (due to blade cutting the abradable sample in an arc) was compensated using a form removal procedure. The surface height was averaged across the width direction to obtain a line. A 2nd order polynomial was then fitted to the radius of the circle as shown in Figure 19. The 2nd order polynomial was found to be sufficient as the surface arc was short. Each line across the surface was then subtracted by the value determined by the 2nd order polynomial, resulting in a surface datumed to its mean height. As a result, the surface profile with the form removed shown in Figure 20 presents the surface shape created by the incursion test, but not how deep this surface was rubbed into.

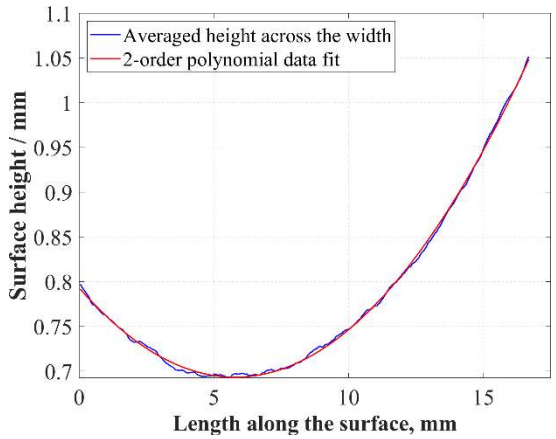

Figure 19 - The surface form along the length of the cut and the fitted 2-nd order polynomial

Several areal surface roughness metrics were calculated using the compensated surface. They are the average height of the selected area, S_a, the root-mean-square height of the selected area, S_q, the maximum peak height of the selected area, S_p, the maximum valley depth of the selected area, S_v, and the height of the selected area (sum of the absolute values of S_p and S_v), S_z.

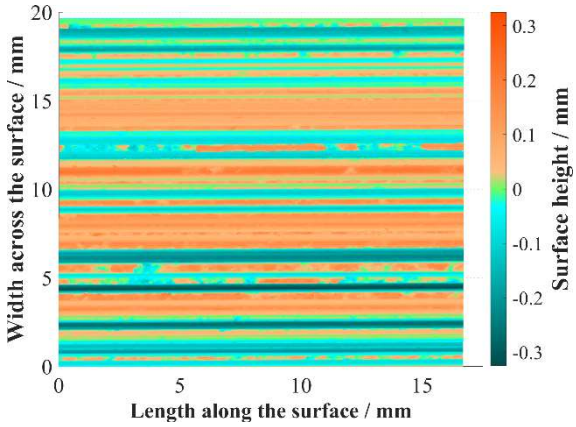

Figure 20 - The tested sample with the form removed

An area dependence study was performed by considering the whole width of the sample and increasing the range of x-coordinates (length along the surface) considered. Based on the results shown in Figure 21 roughness does not change significantly with an increase in the length of the sample considered. This result confirms that the area selected for Alicona analysis is representative of the rubbed surface. This is to be expected as from Figure 20 it appears that the surface height is consistent along the cutting direction and was produced by adhesive and abrasive wear or deformation of the abradable surface by the blade with no signs of macro rupture.

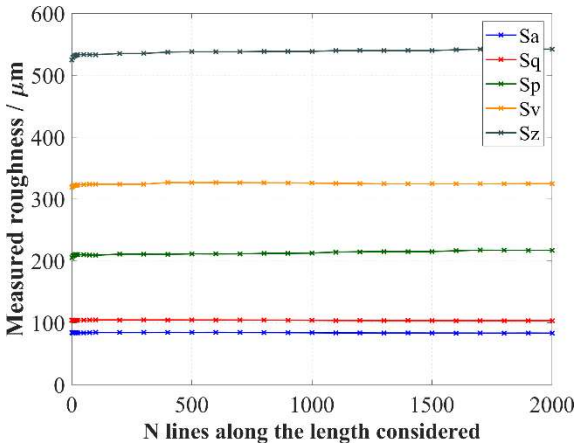

Figure 21 - The area dependence study

4 RESULTS

Results from the three tests outlined in section 2 are presented here. Images of tested blades and abradable samples are shown in Figure 22, Figure 23, and Figure 24. The blade for the test performed at an incursion rate of 0.02µm/pass and blade tip speed of 85m/s (Figure 22) appears to be severely worn and has visible thermal damage on it, while the blades for the tests performed at 0.2µm/pass at blade speeds of both 85m/s (Figure 23) and 170m/s (Figure 24) appear to be relatively undamaged.

Four of the raw blade images obtained using the stroboscopic system (at 0%, 33%, 67% and 100% rub length; time from the start of the test in seconds is indicated on each image) are shown for all three tests in Figure 25, Figure 26 and Figure 27. These images show the visual progression of damage to the blades through time; some adhesions can be observed on a blade by 33% of its respective rub length for all three tests, with the most severe blade edge roughness at the end of a test observed for the test at 0.02µm/pass and 85m/s (Figure 25).

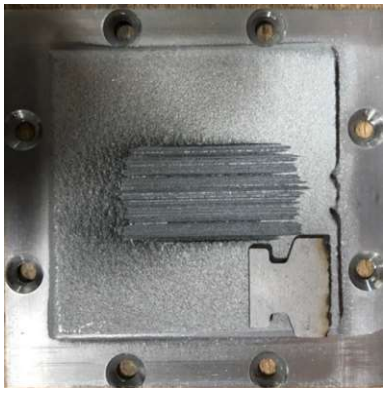

Figure 22 - The tested abradable sample and blade for the test at 0.02µm/pass and 85m/s

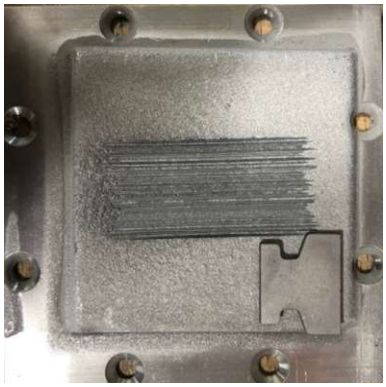

Figure 23 - The tested abradable sample and blade for the test at 0.2µm/pass and 85m/s

Figure 24 - The tested abradable sample and blade for the test at 0.2µm/pass and 170m/s

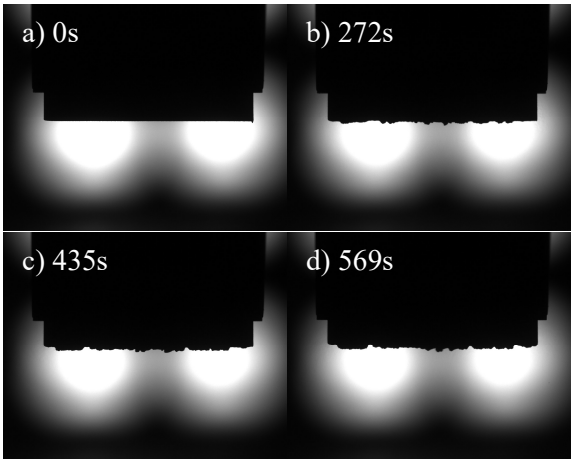

Figure 25 - The raw blade images throughout the test for the test at 0.02µm/pass and 85m/s, images correspond to the rub length of a) 0m, b) 364m, c) 740m, d) 1104m

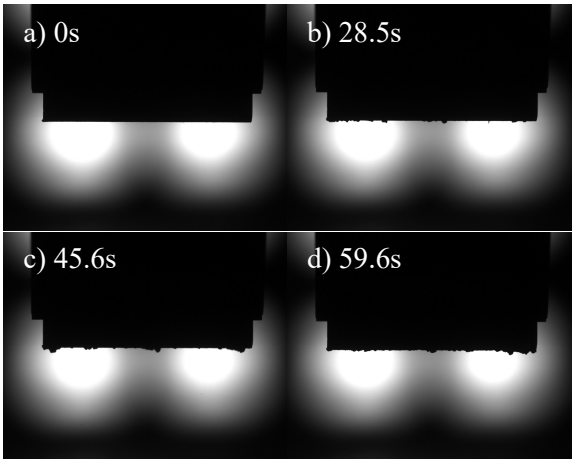

Figure 26 - The raw blade images throughout the test for the test at 0.2µm/pass and 85m/s, images correspond to the rub length of a) 0m, b) 39m, c) 79m, d) 118m

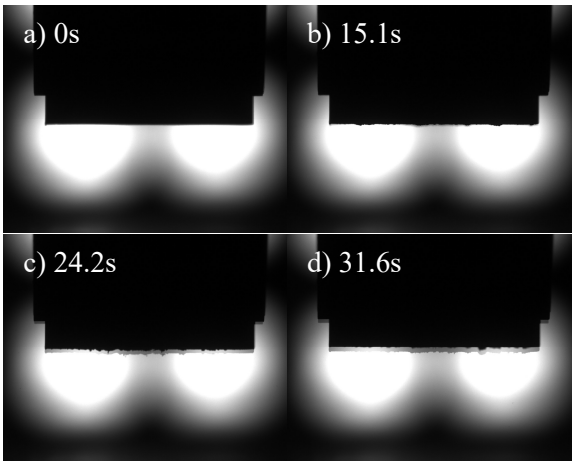

Figure 27 - The raw blade images throughout the test for the test at 0.2µm/pass and 170m/s, images correspond to the rub length of a) 0m, b) 43m, c) 86m, d) 129m

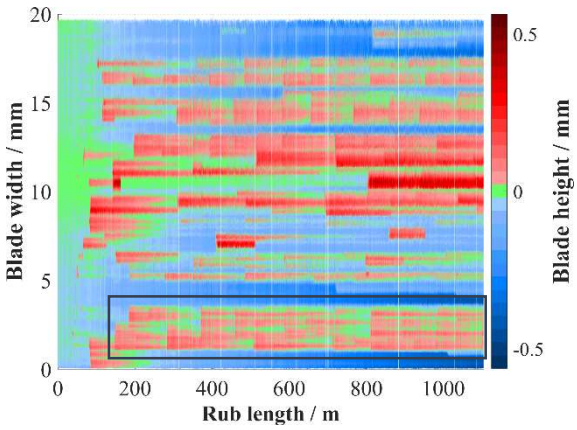

Figure 28 - The blade profile history map for the test at 0.02µm/pass and 85m/s

4.1 Test at 0.02µm/pass and 85m/s

The blade profile history map for the test at 0.02µm/pass and 85m/s can be seen in Figure 28. Simultaneous localised blade wear due to abrasion and localised blade length growth due to adhesion can be observed. In places where adhesions wear off, re-adhesions tend to occur, as can be seen in the area inside of the blue rectangle marked on the figure. In a few places during the test (for example, around the 7.5mm blade width line), the adhesions have rapidly fractured (where red has rapidly changed into green/light blue) and re-adhesions have not immediately reappeared in these places.

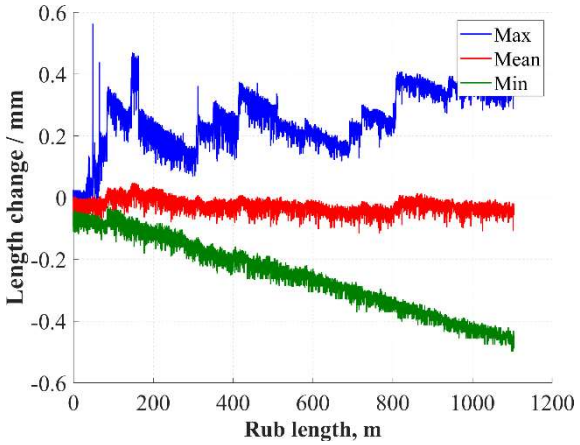

Figure 29 - Max, mean and min results for the test at 0.02µm/pass and 85m/s

The max, mean and min blade length results throughout a test are presented in Figure 29. The maximum value of adhesions remained approximately the same during the test. Blade wear occurred consistently and did not exhibit periodic behaviour. This is in line with the previous observations of wear in Ti (6Al 4V) blades – AlSi-polyester abradables contacts, where for the case, where wear was seen, it was also non-periodic (11). Focusing on adhesions, it can be seen that once an adhesion forms, it starts to gradually wear off, as the maximum value continuously decreases until a larger adhesion initiates and becomes the new maximum.

The post-test abradable surface profile measured using Alicona is given in Figure 30a and a plot showing the comparison of blade profiles constructed following the methodology described in section 3.3 with the averaged Alicona abradable surface profile is shown in Figure 30b. Alicona results in Figure 30b were inverted and the negative of the blade profiles was plotted to ensure that all the plots are shown in the same orientation.

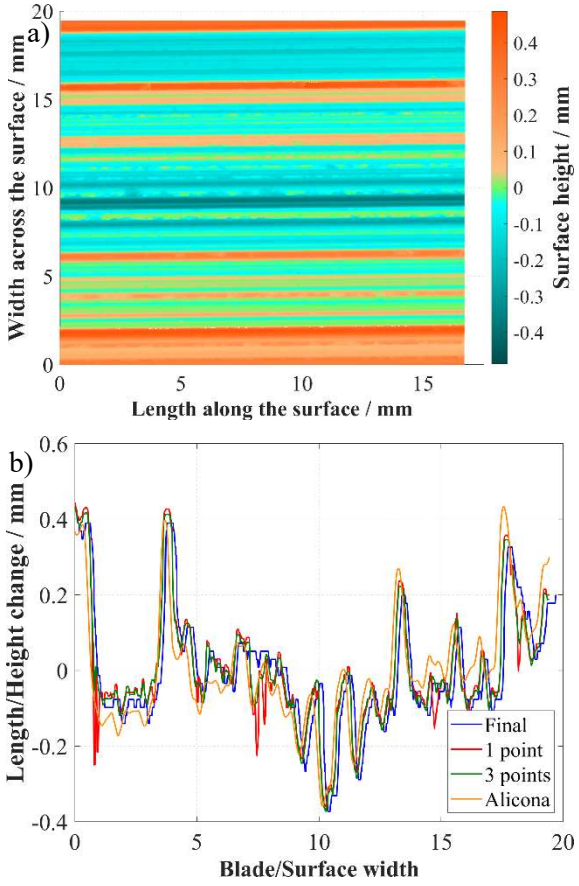

Figure 30 - a) The Alicona measured surface with the form removed, b) the comparison of the Alicona averaged surface profile and the blade-based profiles for the test at 0.02µm/pass and 85m/s

It can be seen in Figure 30b that both the final blade profile and the expected surface profiles based on the previous adhesions on the blade, match well with each other and with the Alicona result. This is because for this test, there was only a very small number of adhesions that fractured, and adhesions tended to gradually wear off instead. This resulted in little to no gaps between the final blade and the abradable surface. Some spikes can be seen in the results for the 1-point blade profile (shown in red), which are not seen on the other three plots. These spikes are due to very long adhesions that existed briefly and have fractured thereafter.

4.2 Test at 0.2µm/pass and 85m/s

Figure 31 shows the blade profile history map for the test at the higher incursion rate of 0.2 µm/pass and speed of 85m/s. For this test, adhesions rapidly fractured more frequently than for the test at 0.02µm/pass and no obvious places of re-adhesions were observed, while the maximum size of adhesions stayed at a comparable value of about 0.5mm as can be seen in Figure 32. No blade wear

is seen, which is confirmed by Figure 32, where the minimum blade length change stays around the zero value. It should be noted, rub lengths for the tests at 0.2µm/pass are an order of magnitude smaller than for the test at 0.02µm/pass, meaning that the blade wear results are hard to directly compare across the tests in terms of absolute magnitudes.

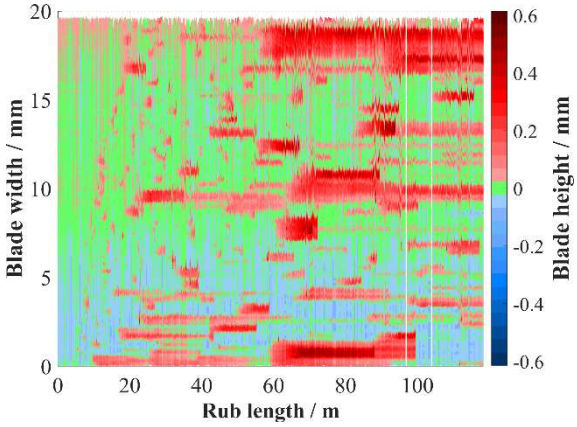

Figure 31 - The blade profile history map for the test at 0.2µm/pass and 85m/s

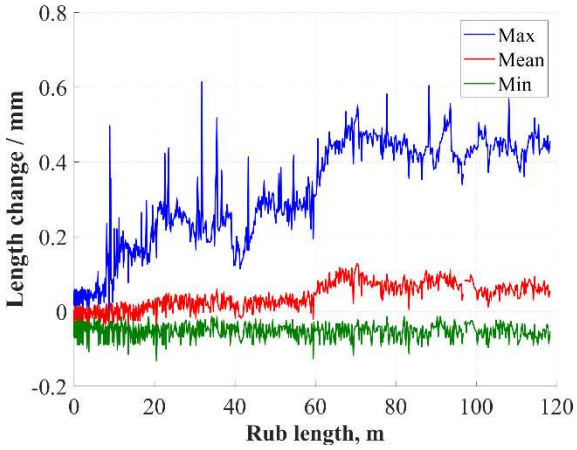

Figure 32 - Max, mean and min results for the test at 0.2µm/pass and 85m/s

The Alicona profile and the comparison of the Alicona and the blade-based profiles are shown in Figure 33. The final blade profile does not match the abradable surface profile at some points along the blade width, while, the 3-points based profile, which considers adhesions that have broken off, shows a very close match with the Alicona result. The 1-point profile has spikes similar to the ones observed for the 1-point based profile in the test at 0.02µm/pass and likewise, these spikes are not seen on the surface profile measured with the Alicona.

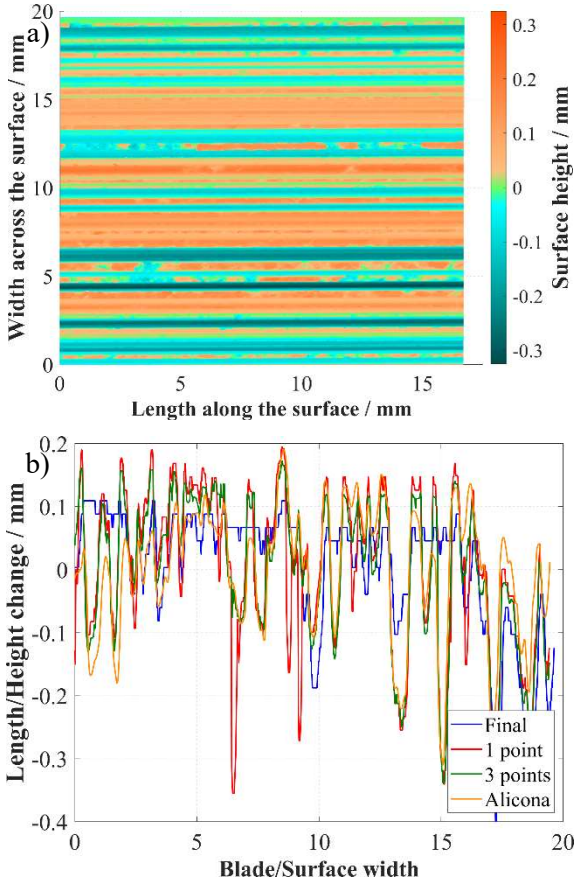

Figure 33 - a) The Alicona measured surface with the form removed, b) the comparison of the Alicona averaged surface profile and the blade-based profiles the test at 0.2µm/pass and 85m/s

4.3 Test at 0.2µm/pass and 170m/s

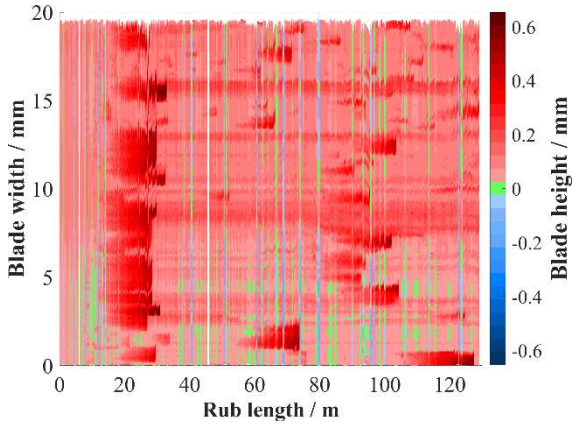

Figure 34 - The blade profile history map for the test at 0.2µm/pass and 170m/s

The blade profile history map for the test at 0.2µm/pass and the higher speed of 170m/s is shown in Figure 34. Similarly, to the test at 0.2µm/pass and 85m/s, multiple adhesions that rapidly fracture and no blade wear can be observed. However, for this test more uniformity is observed

with adhesive pickup seen along the entire blade width.

In Figure 35 a strong periodic behaviour with growth and rapid fracture of adhesions is observed. The flat areas where almost no adhesive growth is observed, are likely due to periods when post fracture, there is a gap between the blade and the sample until the abradable reaches the blade again.

The Alicona profile and the comparison of the Alicona and the blade-based profiles are shown in Figure 36. The comparison between the Alicona and the blade results is similar to the test at 0.2µm/pass and 85m/s, where the final blade profile does not match the Alicona result in some places, while the 3-points based profile shows good agreement as shown in the figure. A single spike around the position of 15mm along the blade width is seen in the 1-point profile, which was not seen on the Alicona measured surface profile, marking the only disparity in the results.

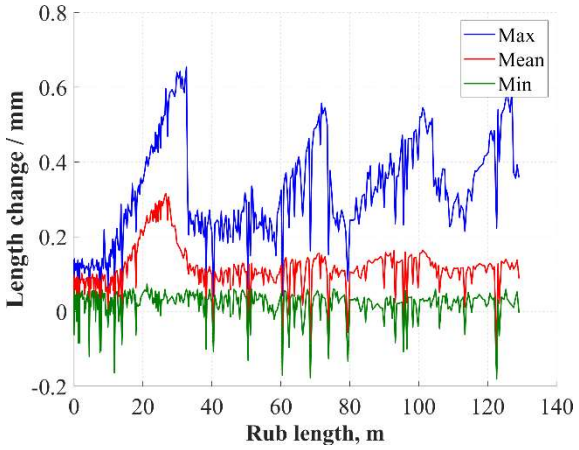

Figure 35 - Max, mean and min results for the test at 0.2µm/pass and 170m/s

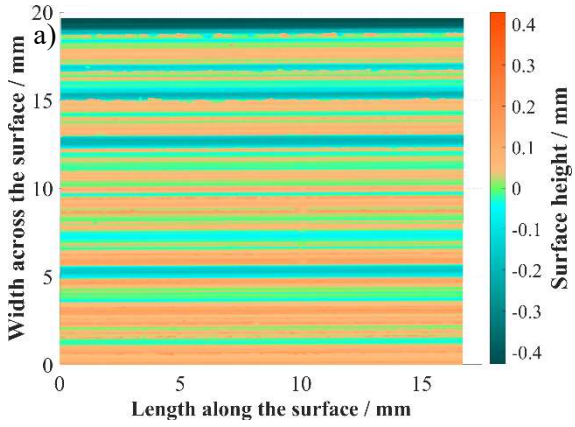

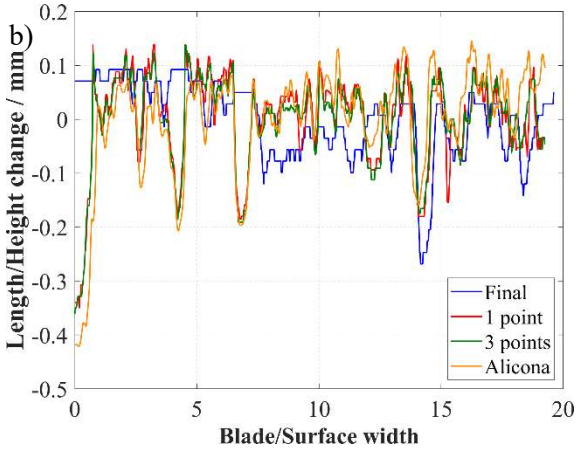

Figure 36 - a) The Alicona measured surface with the form removed, b) the comparison of the Alicona averaged surface profile and the blade-based profiles for the test at 0.2µm/pass and 170m/s

4.4 SEM Results

Backscattered SEM images of blade edge adhesions were obtained for all three tested blades. For the test at 0.02µm/pass and 85m/s, the location of blade wear was also imaged.

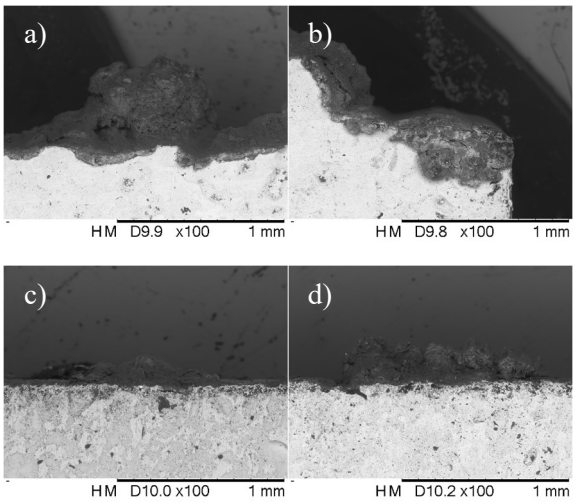

Figure 37 - SEM results a) adhesion for the test at 0.02µm/pass and 85m/s, b) wear for the test at 0.02µm/pass and 85m/s, c) adhesion for the test at 0.2µm/pass and 85m/s, d) adhesion for the test at 0.2µm/pass and 170m/s

It can be seen that for all three tests, adhesions differ in composition to the blade material and are therefore transfer layers from the abradable coating onto the blade. In Figure 37b, it can also be seen that in the location of blade wear, a separate, potentially oxidative layer has formed on the side of the blade.

4.5 Roughness Results

The roughness results for blade profiles and Alicona surface measurements are given in Table 2. Ra, Rq, Rp, Rv and Rz values were generated based on the blade-based profiles, alongside the Alicona averaged surface profile (Alicona averaged). Sa, Sq, Sp, Sv and Sz values were obtained by analysing the full 3D Alicona results (Alicona areal).

The blade and abradable surface roughness at the end of the tests were the highest for the test 0.02µm/pass and 85m/s due to presence of simultaneous wear and adhesions. Very consistent fracture of adhesions for the test at 0.2µm/pass and 170m/s led to the lowest blade roughness at the end of the test. However, it can be seen that Sp and Sz are higher for the abradable surface for this test than for the test at 0.2µm/pass and 85m/s showing that the adhesions cut deeply into the abradable before they fractured.

0.02µm/pass and 85m/s	**Final blade**	**1 point**	**3 points**	**Alicona averaged**	**Alicona areal**
$R_a(S_a)$ / µm	117	114	110	114	116
$R_q(S_q)$ / µm	153	155	151	153	158
$R_p(S_p)$ / µm	373	360	373	359	390
$R_v(S_v)$ / µm	411	443	431	434	487
$R_z(S_z)$ / µm	784	803	804	792	876
0.2µm/pass and 85m/s	**Final blade**	**1 point**	**3 points**	**Alicona averaged**	**Alicona areal**
$R_a(S_a)$ / µm	80	103	95	80	84
$R_q(S_q)$ / µm	104	126	116	100	104
$R_p(S_p)$ / µm	399	354	338	310	325
$R_v(S_v)$ / µm	109	194	171	191	217
$R_z(S_z)$ / µm	509	548	509	501	542
0.2µm/pass and 170m/s	**Final blade**	**1 point**	**3 points**	**Alicona averaged**	**Alicona areal**
$R_a(S_a)$ / µm	57	65	62	70	72
$R_q(S_q)$ / µm	71	87	86	102	104
$R_p(S_p)$ / µm	268	348	371	422	429
$R_v(S_v)$ / µm	92	139	138	146	191[1]
$R_z(S_z)$ / µm	360	487	509	568	621

Table 2 - The comparison of the roughness measures obtained by analysing the captured blade images and the Alicona results for the abradable surfaces for all three tests

[1] Please note that results for $R_p(S_p)$ and $R_v(S_v)$ have been inverted for Alicona results such that $R_p(S_p)$ became $R_v(S_v)$ and vice versa. This was done to keep $R_p(S_p)$ and $R_v(S_v)$ values consistent with the results from blade profiles as a blade peak is an abradable valley and vice versa.

5 DISCUSSION

The results in this study give a real time insight into the blade tip wear mechanisms along an entire blade front, something that has been inferred in previous studies either from post-mortem analysis, or more limited in-situ measurements. Adhesive transfer of material from the liner onto the blade tip was identified as the dominant wear mechanism for the incursion conditions used in this study, which is consistent with the results from previous studies, where similar conditions were investigated (7) (11).

5.1 Analysis of the Adhesion Cyclic Mechanism

The fracture of adhesions was first inferred by Bounazef et al. (8) from post-test blade length measurements, and observed by Fois et al. (10) using a side-on stroboscopic imaging technique. In the latter study only the maximum length of the blade was captured, and it was not possible to determine if adhesions then re-established consistently in the same location, given shadowing due to other adhesions along the blade front.

The results here offer new insights into the cyclic formation and removal of adhesions, which was observed in two of the three performed tests: the test at the lower incursion rate of 0.02microns/pass and the speed of 85m/s and the test at the incursion rate of 0.2microns/pass and the higher speed of 170m/s.

For the test at 0.02microns/pass and 85m/s the cyclic mechanism was driven by the existence of an already adhered material in a given sport. Once an adhesion initiated, peaks grew, and were removed at a broadly consistent rate as shown by the lines extracted from the test in Figure 38. It is also interesting to note, that where previous studies (10) have assumed fracture of the adhered material once a critical length is reached, more gradual wear is also evident for this test. Five individual adhesion events from the 9.3mm line were overlaid onto each other to further illustrate the similar adhesion rates shown in Figure 39a and subsequent gradual wear shown in Figure 39b.

For the test at 0.2microns/pass and 170m/s the cyclic mechanism was driven by an increased overall rate of adhesion formation inferred from Figure 34, where adhesions are a lot more uniform across the entire blade front than for the other two tests. After an existing adhesion fractured, a new one easily initiated in the same location along the blade width once the blade returned into the contact with the abradable surface.

It was then concluded that the cyclic process of adhesion formation and removal is greatly influenced by the general probability of adhesion formation in a given location on the blade, with this probability influenced by two factors: existence of an already adhered material in that location as in the example of the test at 0.02microns/pass and 85m/s; and increased blade tip speed as in the example of the test at 0.2microns/pass and 170m/s.

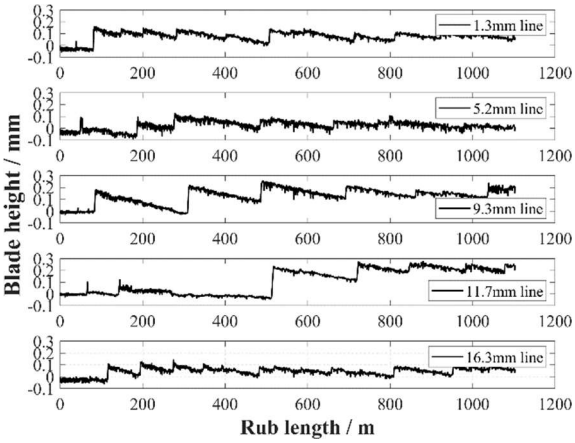

Figure 38 - Lines extracted for the test at 0.02µm/pass and 85m/s at 1.3mm, 5.2mm, 9.3mm, 11.7mm and 16.3mm blade width

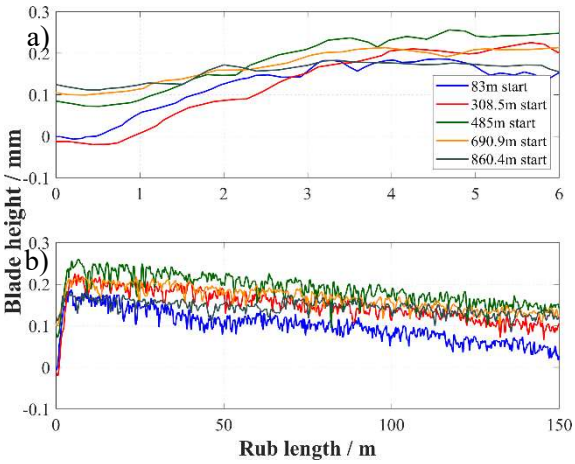

Figure 39 - Individual adhesion events overlaid onto each other for the 9.3mm line showing a) adhesive growth phase, b) adhesive growth and subsequent wear phase

5.2 Simultaneous Adhesion and Wear

In the test at 0.02µm/pass and 85m/s (Figure 28) wear of the blade and adhesions occurred simultaneously at different points along the blade front. This phenomenon has been well documented (8; 9; 20) with Fois et al. (20) demonstrating that it occurs as a consequence of localities in the material microstructure, preventing thermal diffusion, leading to a local hot spot on the surface. This hot

spot is sufficient to lead to melt wear of the blade, where adhesion of the aluminium-silicon liner to the blade occurs elsewhere.

Previously it was assumed that the wear mechanism was continuous and progressive, and once thermal wear of the blade was initiated, this continued (20). Taking the results shown in Figure 28 as an example, this is not the case. As shown in the Figure, whilst between 0 and 4mm along the blade width two areas of progressive wear occurred, at approximately 7.5mm and 15mm, blade wear occurred for a period before adhesion initiated. Whilst at 7.5mm adhesion was short lived, with wear re-establishing, continued adhesion cycles occurred at 15mm.

The variation observed is likely due to changes in the thermal diffusivity of the material, caused as localities in microstructure are either removed, or indeed come into increased proximity of the blade tip, given the established connection between material microstructure and wear mechanism (20), and that the incursion event represents a process through which material is progressively removed from the liner. This gives further insight into the transient nature of wear in abradable lining sealing systems identified by multiple authors (7; 8; 12).

5.3 Comparison of Tests at Different Incursion Rates

Fracture rather than gradual wear of adhesions was observed at the higher incursion rate as seen by comparing Figure 28 and Figure 31, both at the speed of 85m/s, but at incursion rates of 0.02µm/pass and 0.2µm/pass respectively. This result is consistent the study by Watson et al. (11), where periodic adhesion and fracture was also seen for similar test conditions. It was previously shown that observed forces generally increase with an increase in the incursion rate (11) for tests with AlSi-polyester abradables, which is what likely drives the higher fracture of adhesions.

Results also show that fracture of adhesions leads to gap formation between a blade and a corresponding abradable as can be seen from Figure 30 and Figure 33. Gap formation is undesirable as this leads to aerodynamic losses and decreased efficiency of aero-engine compressors.

Specifically with respect to gaps due to fracture of adhesions, it can be seen that an abradable surface at the end of a given test is as a product of the adhesions and wear history, as opposed to being solely dependent on the instantaneous blade form. These findings further support the idea that post-test blade length and weight measurements commonly used in literature (7; 8; 9; 10; 11; 12; 14) are not always representative of the overall adhesive transfer during a test and hence, are insufficient to fully quantify the severity of wear mechanisms present under certain testing conditions.

5.4 Adhesion Measurements

Five lines were extracted from the blade profile history maps for each test (Figure 28, Figure 31 and Figure 34) at the following blade width locations for adhesion rate and peak heights calculations to aid the comparison of tests at different speeds:

Test at 0.02µm/pass and 85m/s: 1.3mm, 5.2mm, 9.3mm, 11.7mm, 16.3mm

Test at 0.2µm/pass and 85m/s: 0.2mm, 2.6mm, 9.5mm, 13.3mm and 18.2mm

Test at 0.2µm/pass and 170m/s: 0.6mm, 4.0mm, 7.1mm, 12.5mm, 15.9mm

5.5 Comparison of Tests at Different Speeds

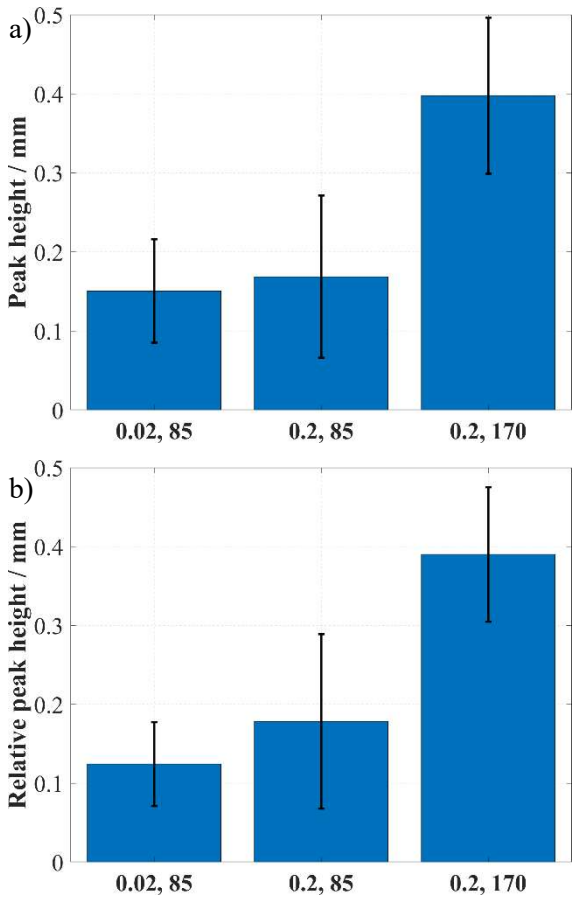

Figure 40 - Calculated a) peak heights and b) relative peak heights for all three tests

Comparing Figure 31 and Figure 34, both at an incursion rate of 0.2 microns per pass, but at speeds of 85m/s and 170m/s respectively, it is clear that the wear mechanism has changed with speed, although the final results in terms of roughness are similar. It can be seen that the average length of adhesion peaks is higher (Figure 40) and adhesive pick-up and fracture more consistent at the higher blade speed, and additionally initiation of adhesion is also earlier (Figure 41). This result is consistent with the early study undertaken by Borel et al. (7) where for an AlSi-plastic coating, with a low melting plastic, frictional heating was observed to increase with blade speed, with adhesion increasing before ultimately a transition to blade melting occurred. Similar rises in contact temperature with blade speed for an AlSi-plastic abradable were also measured by Watson et al. (11), where the limited change in overall test outcome in terms of final adhesion and liner grooving was also noted.

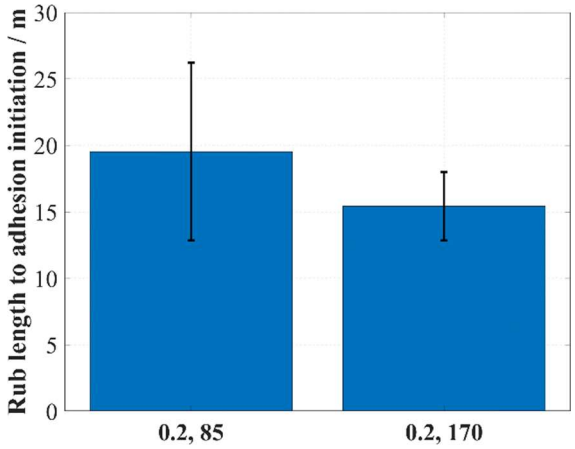

Figure 41 - Comparison of rub length to the initiation of first adhesion for tests 2 and 3

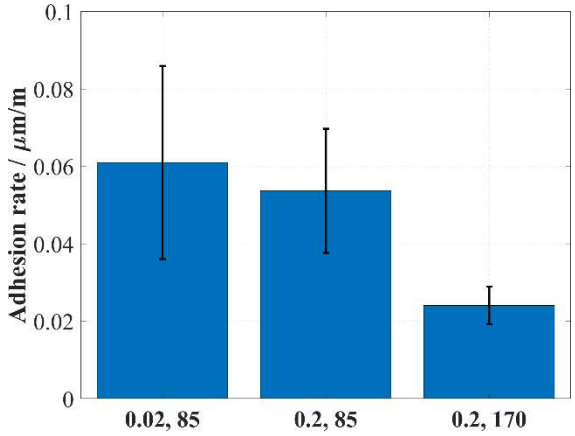

Figure 42 - Calculated adhesion rates with respect to the rub length for all three tests Despite the increased likelihood of adhesive transfer and more consistent pick-up at the higher speed, adhesion rate was seen to drop with speed (Figure 42). This result is, however, consistent with the results of Fois et al. (10) obtained for the tests with AlSi-hBN abradables, where adhesion rate at a given incursion condition was seen to drop with blade speed, with this drop associated with decreased contact residency time and higher striking impact energy.

6 CONCLUSION

Three tests have been performed to investigate wear mechanisms observed during Ti (6Al 4V) blades against AlSi-polyester abradables rubs. The incursion rates of 0.02µm/pass and 0.2µm/pass and the blade tip speeds of 85m/s and 170m/s were considered. The incursion rate was found to be the main driving factor for the wear mechanisms observed during a test with simultaneous adhesion and wear observed at the lower incursion rate of 0.02µm/pass.

For both tests at the higher incursion rate of 0.2µm/pass only adhesions were present. Comparing to the test at the lower incursion rate, higher number of adhesion fracture events was observed for the tests at the higher incursion rate, leading to gaps between the final blade profile and corresponding abradable surfaces.

The wear mechanism was also observed to change with speed, as was seen by comparing results between tests at 0.2 µm/pass incursion rate, but different speeds of 85m/s and 170m/s. A much more uniform formation and fracture of adhesions along the entire blade width, larger average adhesions height and quicker initiation of adhesion was observed for the test at the higher speed.

Further testing will be performed to better understand the wear mechanisms involved in contacts between Ti (6Al 4V) blades and AlSi-polyester abradables. It will include force and temperature data from the dynamometer and the pyrometer installed on the rig. The speed, the incursion rate and the abradable hardness effects on test results and the comparison of different batches of abradables of the same nominal hardness are the parameters, which were identified to be of the most interest for future work.

7 BIBLIOGRAPHY

1. **Hopkins, N P.** *Abradable coatings - From black art, to materials science.* s.l. : Swansea University E-Theses, 2007.

2. *Friction and wear behaviour and abradability of abradable seal coating.* **Yi, M, et al.** s.l. : Wear, 1999, Vol. 231.

3. *Investigation of abradable seal coating performance using scratch testing.* **Ma, X and Matthews, A.** s.l. : Surface and Coatings Technology, 2007, Vol. 202.

4. *Interactions between blades and abradable coatings: A numerical approach considering geometrical nonlinearity* . **Xiao, Jiaguangyi, et al.** s.l. : International Journal of Mechanical Sciences, 2021, Vol. 191.

5. *Reduced order modeling of blades with geometric nonlinearities and contact interactions.* **Delhez, E, et al.** s.l. : Journal of Sound and Vibration, 2021, Vol. 500.

6. *Abradable coating removal in turbomachines: a macroscopic approach accounting for several wear mechanisms.* **Berthoul, B, et al.** s.l. : ASME Turbo Expo 2015: Turbine Technical Conference and Exposition, 2015.

7. *The Wear Mechanisms Occuring in Abradable Seals.* **Borel, M O, Nicoll A R, Schlapfer H W and K, Schmid R.** Winterthur : Surface and Coatings Technology, 1989, Vol. 39/40.

8. *The wear, deterioration and transformation phenomena of abradable coating BN–SiAl–bounding organic element, caused by the friction between the blades and the turbine casing.* **Bounazef, M, Guessasma, S and B, Ait Saadi.** s.l. : Materials Letters, 2004, Vol. 58.

9. *High speed wear testing of an abradable coating.* **Stringer, J and Marshall, M B.** s.l. : Wear, 2012, Vols. 294-295.

10. *Adhesive transfer in aero-engine abradable linings contact.* **Fois, N, Stringer, J and Marshall, M B.** 1-2, s.l. : Wear, 2013, Vol. 304.

11. *Wear mechanisms at the blade tip seal interface.* **Watson, M and Marshall, M B.** s.l. : Wear, 2018, Vols. 404-405.

12. *Evaluation of an AlSi-polyester abradable seal coating performance using high-temperature and high-velocity abrasion tests.* **Zhang, N, et al.** s.l. : Proceedings of the Instittution of Mechanical Engineers, Part J: Journal of Engineering Tribology, 2015.

13. *Material transfer behaviour between a Ti6Al4V blade and an aluminium hexagonal boron nitride abradable coating during high-speed rubbing.* **Xue, W, et al.** s.l. : Wear, 2015, Vols. 322-323.

14. *Effects of blade material characteristics on the high-speed rubbing behavior between Al-hBN abradable seal coatings and blades.* **Xue, W, et al.** s.l. : Wear, 2018, Vols. 410-411.

15. *Mechanisms of incursion accommodation during interaction between a vibrating blade and an abradable coating.* **Mandard, R, et al.** s.l. : Wear, 2015, Vols. 330-331.

16. *An advanced experimental method and test rig concept for investigating the dynamic blade-tip/casing interactions under engine-like mechanical conditions.* **Nitschke, S, et al.** s.l. : Wear, 2019, Vols. 422-423.

17. **Watson, M.** *Modifications of blade tips in abradable contacts.* Sheffield : The University of Sheffield, 2017.

18. *An Experimental Investigation of Temperatures Due to Rubbing at the Blade-Seal Interface in an Aircraft Compressor.* **Emery, A F, et al.** s.l. : Wear, 1983, Vol. 91.

19. *Criteria for analysis of abradable coatings.* **Wang, H.** s.l. : Surface and Coatings Technology, 1996, Vol. 79.

20. *The influence of material properties on the wear of abradable materials.* **Fois, N, Watson, M and Marshall, M B.** s.l. : Proceedings of the Institution of Mechanical Engineers, Part J: Journal of Engineering Tribology, 2017, Vol. 231.

21. **Stout, K J.** *Development of the Methods for the Characterisation of Roughness in Three Dimensions.* 2000.

22. *Investigation of high-speed abrasion behavior of an abradable seal rubber in aero-engine fan application.* **Xuan, H, et al.** 4, s.l. : Chinese Journal of Aeronautics, 2017, Vol. 30.

A. APPENDIX A – DISK EDGE EXTRACTION FOR USE IN REFERENCING

The disk edge extraction was done as part of the blade profiles referencing procedure described in section 3.2.

At the start of the data processing, the user is asked to select 4 data points, which create a limit for the disk edges on the left and the right of the blade as shown in Figure 43. Some space is left to the left and the right of the actual disk edge to allow for some variation in the position of the disk and the blade on the images in a dataset. All the vertical position indexes for data points on the left of the blade are averaged to give a y-position index for the disk edge to the left of the blade. The same procedure is done for the disk edge to the right of the blade. These two values are then averaged to obtain, the average observed projection of the disk edge for this image, l_{do}.

Figure 43 - The reference lines selected on the original image after it was cropped

These values are y-positions of the disk edge, projected onto the camera. P_d, is, therefore equal to the vertical positions converted from the number of pixels to microns added to the unobserved part from the centre of the disk to the field of view of the camera limit, l_{du}. l_{du} is found by using the assumption that when the disk edge and the blade edge are perpendicular to the camera, the projected edge length is the longest it could appear and $P_{d(max)} = l_d$. Also, it is assumed, that at least one image in the dataset is very close to the perfectly perpendicular position, which is highly probable. It was attempted to justify this assumption by plotting the histograms of the edge reference values (pixel number value from the top of a cropped image) for a spin-up of the spindle with no incursion into an abradable and for one of the incursion tests. The histograms are shown in Figure 44.

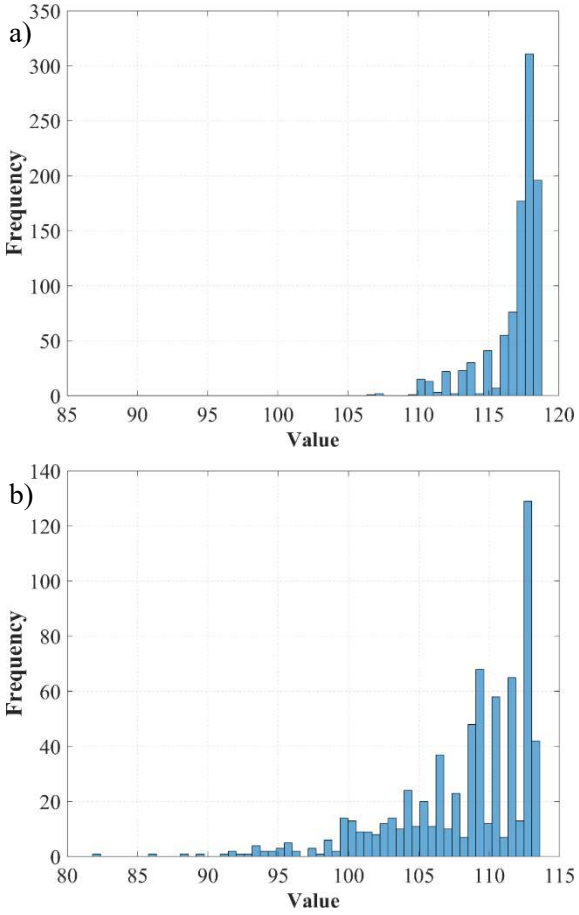

Figure 44 - The histogram of disk edge reference values for a) a test with no incursion, b) one of the incursion tests

For a perfectly selected delay time, values are expected to deviate around the position where the blade is perpendicular to the camera, and thus, where the disk edge is seen as maximum. Then the distribution is expected to look like a half of a normal distribution (truncated at where the mean value would be). That is what is approximately seen on both histograms with both histograms being truncated after a certain value. The mean value is slightly deviated from the rightmost edge for both histograms, most likely because of the imperfection in the selection of the strobe delay time. The shape of the histograms suggests, that for both cases, the maximum acquired disk edge value is the actual maximum value and so, it could be used to reference all other captured images.

Then by finding the maximum observed projection of the disk edge, $l_{do(\max)}$

$$P_{d(\max)} = l_{du} + l_{do(\max)} = l_d$$

Equation 6

Then

$$l_{du} = l_d - l_{do(\max)}$$

Equation 7

Thus, it is possible to convert l_{do} values into P_d values for all the analysed images.

$$P_d = l_{du} + l_{do}$$

Equation 8

Similarly, it is possible to convert all the observed blade edge profiles, l_{bo}, into P_b and convert back from l_b to the observed blade profiles after referencing, $l_{bo(ref)}$, which is the last step of the referencing procedure.